Check for updates

Synergistic design of a graphene oxide-mediated polyaniline/α-Fe₂O₃ ternary heterostructure: advancing photocatalytic degradation and adsorption efficiency†

Iftekhar Ahmad,‡[a] Mohammad Saud Athar,‡[a] Mohammad Muneer, [iD] *[a]
Hatem M. Altass,[b] Raad Felemban[c] and Saleh A. Ahmed [iD] *[b]

With the growing threat of organic pollutants in water bodies, there is an urgent need for sustainable and efficient water decontamination methods. This research focused on synthesizing a novel Z-scheme ternary heterostructure composed of graphene oxide (GO)-mediated polyaniline (PANI) with α-Fe₂O₃ and investigated its potential in brilliant green (BrG) and ciprofloxacin (CIP) degradation tests under visible light. The ternary composite demonstrated exceptional photocatalytic activity, with the optimized 10% PANI/GO/α-Fe₂O₃ (10PGF) photocatalyst achieving 99.8% degradation of BrG in 25 min and 93% degradation of CIP in 90 min of irradiation. The 10PGF composite achieved rate constants of 0.222 min⁻¹ for BrG and 0.0295 min⁻¹ for CIP. The rate constant for BrG degradation was 15 and 10 times faster than that for PANI and α-Fe₂O₃, respectively, while CIP was degraded 8.9 and 6.1 times faster. The degradation of the pollutants was facilitated by both $O_2^{\cdot-}$ and $^{\cdot}OH$, as confirmed by capturing active species, a nitroblue tetrazolium test and use of a PL terephthalic acid probe. The proposed Z-scheme mechanism elucidated charge carrier movements and active species involvement, revealing the enhanced photocatalytic performance of the ternary composite. The 10PGF ternary composite demonstrated exceptional recyclability over five repeated cycles, with XRD analysis confirming no structural changes in the material. Moreover, adsorption studies were also performed, which showed a strong correlation ($R^2 = 0.974$) with Langmuir isotherms and that pseudo-second order kinetics was followed.

1. Introduction

Organic pollutants in water contribute to significant risks for both aquatic ecosystems and human health.[1–3] These pollutants comprise a diverse range of compounds, including industrial dyes, pharmaceuticals and personal care products, which are resistant to conventional water-treatment methods.[4–6] Brilliant green, EBT, methyl orange, *etc.*, which are synthetic dyes commonly used in the textile industry,[7,8] and drug molecules, particularly antibiotics, are common water contaminants. Metronidazole (MNZ) (2-methyl-5-nitroi-

ᵃDepartment of Chemistry, Faculty of Science, Aligarh Muslim University, Aligarh 202002, India. E-mail: m.muneer.ch@amu.ac.in
ᵇDepartment of Chemistry, Faculty of Science, Umm Al-Qura University, 21955 Makkah, Saudi Arabia. E-mail: saahmed@uqu.edu.sa
ᶜResearch Laboratories Unit, Faculty of Science, Umm Al-Qura University, 21955 Makkah, Saudi Arabia

midazole-1-ethanol) is a common antibiotic used to treat infections caused by anaerobic bacteria, *Bacteroides*, and protozoa, and ciprofloxacin, a broad-spectrum antibiotic widely prescribed in human and veterinary medicine, are leading examples of organic pollutants frequently detected in aquatic environments.[9,10] These are known to persist in water bodies, exerting detrimental effects on aquatic organisms, disrupting ecological balance, and potentially compromising human health through bioaccumulation. Photocatalysis has emerged as a promising approach for mitigating the adverse effects of these organic pollutants in water.[11–13] By harnessing the energy of light, photocatalysts can initiate advanced oxidation processes (AOPs) to degrade organic contaminants into harmless byproducts such as CO_2 and H_2O.[14] This environmentally benign process offers several advantages, including high efficiency, selectivity, and the ability to operate under mild conditions without generating harmful byproducts or secondary pollutants. TiO_2 and ZnO are two materials widely explored for their photocatalytic efficacy when exposed to UV light.[15] TiO_2 and ZnO possess wide bandgap energies, which allow them to absorb UV light and generate electron–hole pairs for

photocatalytic reactions.[16–18] However, their limited absorption of visible light restricts their application in sunlight-driven photocatalysis, which comprises a significant portion of the solar spectrum.[19] This limitation has inspired the development of visible light-responsive photocatalysts, capable of harnessing energy from a broader range of the solar spectrum for pollutant degradation.

In recent years, significant attention has been directed towards the utilization of α-Fe$_2$O$_3$ (hematite) as a photocatalyst for environmental remediation.[20,21] Hematite possesses a narrow bandgap in the range of 2.0–2.2 eV, which positions it as a potential candidate for visible light-driven photocatalysis.[22] The utilization of α-Fe$_2$O$_3$ in photocatalysis offers several advantages. Firstly, hematite is abundantly available and cost-effective, making it a sustainable option for large-scale environmental applications.[23] Additionally, hematite exhibits excellent chemical stability and low toxicity, further enhancing its appeal for water purification processes.[24] Furthermore, α-Fe$_2$O$_3$ based photocatalysts have been reported to demonstrate high efficiency in degrading various organic pollutants, including dyes, pharmaceuticals, and pesticides.[25] Despite its benefits, the practical use of α-Fe$_2$O$_3$ in photocatalysis is inhibited by drawbacks, such as the quick recombination of electron–hole pairs and low charge-carrier mobility.[26] To address these challenges, researchers have focused on strategies to improve the photocatalytic performance of hematite-based materials. One approach involves surface-modification techniques, such as doping and surface functionalization, to tailor the electronic structure and surface properties of α-Fe$_2$O$_3$, further enhancing its photocatalytic performance.[27] Another very important approach is the design and fabrication of α-Fe$_2$O$_3$ based heterostructures and composites, which can enhance charge separation and facilitate interfacial charge transfer.[28] The design of α-Fe$_2$O$_3$-based heterostructures involves integrating hematite with other semiconductor materials to create interfaces with enhanced charge separation and transfer capabilities.[29] In addition to these composites, α-Fe$_2$O$_3$ based ternary composites have been developed by incorporating into hematite carbon-based nanomaterials (*e.g.*, GO, carbon nanotubes).[30] GO is considered an effective mediator in photocatalysis due to its extensive surface area and conductive nature, which allow it to enhance the separation and transportation of photogenerated charge carriers.[31] Additionally, GO can broaden the light absorption range of semiconductors, making it a valuable component in designing advanced photocatalytic systems for environmental applications.[32,33] In this study, we synthesized and characterized a novel Z-scheme ternary heterostructure composed of PANI, GO, and α-Fe$_2$O$_3$, aiming to elucidate its potential for the degradation of recalcitrant organic compounds. In the field of photocatalysis, PANI has emerged as a promising material due to its ability to facilitate charge transfer. It is a conductive organic polymer valued for its high electrical conductivity, straightforward synthesis, and environmental stability, with its conductivity primarily being due to delocalized π-electrons along the polymer chain that enable efficient charge transport.[34,35] Utilizing comprehensive characterization methods and mechanistic analyses, the study aims to elucidate the synergistic interactions and charge transfer processes that enhance the photocatalytic activity of our designed PANI/GO/α-Fe$_2$O$_3$ ternary composite catalyst. The Z-scheme mechanism, which involves the transfer of photogenerated electrons between two different semiconductors *via* GO, has been discussed to elucidate the underlying mechanisms governing the enhanced photocatalytic activity of the ternary composite. Adsorption studies utilizing the optimized PANI/GO/α-Fe$_2$O$_3$ composite were also performed to evaluate its effectiveness in removing brilliant green dye, thereby demonstrating its effectiveness for pollutant removal from water.

2.   Experimental details

Chemical requirements, materials characterization, active species generation experiments and adsorption experiments are given in the ESI (sections S2.1, S2.2, S2.3, S2.4).†

2.1.   Preparation of pure GO, α-Fe$_2$O$_3$ and PANI

Graphene oxide (GO) was synthesized using a modified Hummers' method, following the procedure detailed in our previous work.[31] α-Fe$_2$O$_3$ was prepared through a hydrothermal technique. In this process, 10 mL of a 2.0 M aqueous FeCl$_3$·6H$_2$O solution was mixed with 20 mL of 1,2-propanediamine and stirred continuously with a magnetic stirrer for 1 h. The mixture was subjected to hydrothermal treatment at 160 °C for 20 h, followed by cooling to room temperature. The resultant material was washed with water and ethanol, and then dried in an oven at 70 °C for 12 h. PANI was fabricated through oxidative polymerization of aniline, using ammonium persulfate as the oxidant. A 0.1 M ammonium persulfate solution was prepared in distilled water and gradually added to a 0.1 M aniline solution in HCl. The mixture was stirred for 12 h at 25 °C, producing a deep green precipitate, which was then washed with distilled water and acetone, and dried at room temperature.

2.2.   Synthesis of PANI/GO/α-Fe$_2$O$_3$ heterostructure

A fixed amount of previously prepared GO was ultrasonically dispersed in 50 mL of water to ensure a uniform mixture. A fixed amount of α-Fe$_2$O$_3$ was then gradually added to the solution, followed by continuous stirring for 1 h. Afterward, 10 wt% of PANI, relative to the combined weight of GO and α-Fe$_2$O$_3$, was added, and the mixture was stirred for 2 h at 80 °C. The final step involved cooling the mixture, and thoroughly washing and then drying the product at 70 °C for 12 h. The same method was used to synthesize a series of x-PANI/GO/α-Fe$_2$O$_3$ composites, referred to as x-PGF, where "x" represents the different weight percentages of PANI (5, 10, 30, and 40 wt%). Additionally, a 10 wt% PANI/α-Fe$_2$O$_3$ binary composite was synthesized without the inclusion of GO, and this was labelled as 10GF.

2.3. Photocatalytic activity

The photocatalytic efficiency of the synthesized samples was assessed by measuring the degradation of brilliant green (BrG) and ciprofloxacin (CIP) under a visible light source (a 500 W halogen lamp). BrG (200 mL, 15 ppm) and CIP (200 mL, 20 ppm) solutions were separately placed in a photoreactor, each containing 0.9 g L^{-1} photocatalyst. To ensure even dispersion, the mixture was sonicated (15 min) and then stirred in the dark (20 min), with a continuous supply of air during irradiation. Samples were taken at regular intervals, centrifuged for 10 min to remove residual material, and analyzed for absorbance changes using a UV-vis spectrophotometer. The total percentage of contaminants degraded was calculated using the formula $D(\%) = (C_0 - C_t)/C_0 \times 100$, where C_0 and C_t denote the initial and final pollutant concentrations, respectively. Additionally, the study explored the effect of varying BrG dye concentrations (5 to 35 ppm) using 0.9 g L^{-1} 10PGF composite, as well as the impact of different 10PGF amounts (0.3–1.8 g L^{-1}) on the degradation of a 15 mg L^{-1} BrG dye solution.

3. Results and discussion

3.1. XRD analysis

X-ray diffraction (XRD) analysis is essential for understanding the crystallographic structure of materials by identifying distinct diffraction patterns associated with specific interplanar spacing, as illustrated in Fig. 1. PANI generally shows broad diffraction peaks in the range of 15–25°, indicative of its semi-crystalline structure, which is largely amorphous in nature.[36] Specific diffraction angles for PANI are observed at 14.95°, 20.07°, and 25.26°, corresponding to the (121), (310), and (003) crystallographic planes, respectively.[37] GO displays prominent peaks at around 10.87° and 24.11°, which correspond to the

(001) and (002) planes. These peaks are characteristic of the layered structure of GO and reflect the interlayer spacing due to the presence of oxygen-containing functional groups.[38] Pure α-Fe$_2$O$_3$ exhibits distinct, well-defined peaks at 2θ values of 24°, 33°, 35°, 40°, 49°, 54°, 62°, and 64°, corresponding to the (012), (104), (110), (113), (024), (116), (214), and (300) planes, respectively. These peaks confirm the hematite phase of α-Fe$_2$O$_3$, which is consistent with the JCPDS file No. 33-0664.[39] In the α-Fe$_2$O$_3$/PANI binary composite, the characteristic peaks of PANI are not visible, likely because the amorphous nature of PANI is overshadowed by the crystalline structure of α-Fe$_2$O$_3$. Slight modifications in the diffraction peaks of α-Fe$_2$O$_3$ are observed, suggesting interactions between α-Fe$_2$O$_3$ and PANI that slightly alter the crystal structure of α-Fe$_2$O$_3$, without introducing new phases or significantly affecting its crystallinity. The XRD pattern of the PGF ternary heterostructure is predominantly characterized by the crystalline peaks of α-Fe$_2$O$_3$. This indicates that the structural integrity and crystallinity of α-Fe$_2$O$_3$ are the dominant features of the composite material. The absence of noticeable peaks for PANI and GO in the ternary composite is likely due to their weak intensity and amorphous nature.

3.2. FTIR and Raman analysis

The synthesized materials were further characterized by Fourier transform infrared (FTIR) spectroscopy to identify their bonding nature and functional moieties. The spectra for pure GO, α-Fe$_2$O$_3$, and PANI, as well as their composite structures, are displayed in Fig. 2. GO shows several characteristic peaks, including those for OH groups appearing at 3500–3400 cm^{-1}, with C–H bonding confirmed by peaks at 2920–2840 cm^{-1}, while C=O stretching is indicated by a peak at 1726 cm^{-1}. Additionally, the C=C bonds in GO are represented by a peak at 1611 cm^{-1}, while the peaks between 1300 and 1000 cm^{-1} correspond to epoxy and carboxyl func-
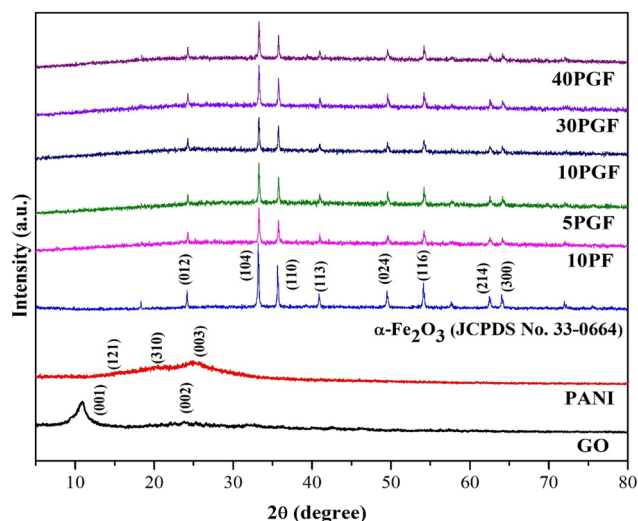

Fig. 1 XRD patterns of pure GO, PANI, and α-Fe$_2$O$_3$, the 10PF binary composite and the PGF ternary composites.
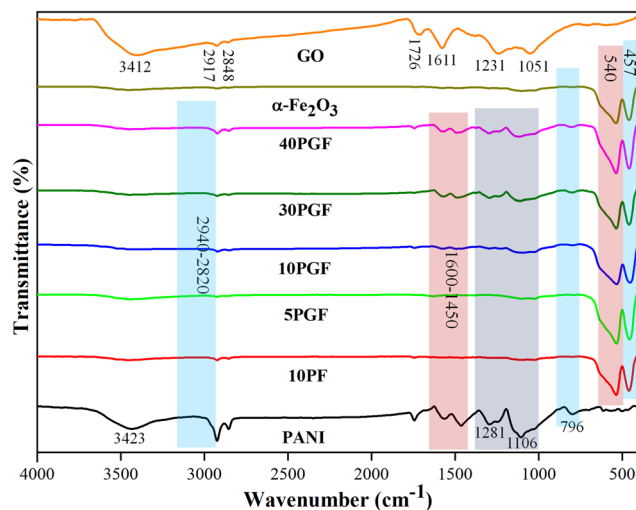

Fig. 2 FTIR spectra of pure GO, PANI, and α-Fe$_2$O$_3$, the 10PF binary composite and various PGF ternary composites.

tional groups.[40] For PANI, the FTIR spectrum exhibits a characteristic peak at 3487 cm^{-1}, which indicates N–H stretching vibration. Peaks within the 3160–3040 cm^{-1} range are associated with the aromatic $=$C–H group, while the peaks in the 2940–2820 cm^{-1} range are indicative of aliphatic C–H groups. Additionally, peaks in the 1600–1450 cm^{-1} range correspond to the C$=$N and C$=$C units present in PANI.[41] Additional distinctive absorption bands in PANI include peaks at 1281 and 1106 cm^{-1} corresponding to C–N stretching and C–H bending vibrations, respectively. A peak at 796 cm^{-1} is attributed to the out-of-plane C–H vibrations of the benzenoid unit.[42,43] In the case of pure α-Fe$_2$O$_3$, two significant peaks in the low wavenumber region, at 540 cm^{-1} and 457 cm^{-1}, indicated stretching and bending vibration modes of the Fe–O group.[44]

Furthermore, Raman spectroscopic analysis was performed to study the intermolecular vibrations in the synthesized photocatalyst. Fig. S1† shows the Raman spectra of α-Fe$_2$O$_3$, PANI, 10PF and 10PGF in the wavenumber range of

200–1500 cm^{-1}. The Raman bands corresponding to the wavenumbers 220, 243, 285, 403, 491, 601 and 1310 cm^{-1} were observed in the spectra of α-Fe$_2$O$_3$. The bands observed at wavenumbers 414, 523, 573, 611, 639, 807, 1182, 1237, 1323, 1339 and 1390 cm^{-1} were assigned to PANI.[45] The spectrum of the 10PF binary composite clearly indicates peaks corresponding to both α-Fe$_2$O$_3$ and PANI. Furthermore, an additional peak was also observed in the spectrum of the ternary composite at 1473 cm^{-1}, indicating the successful incorporation of GO.

3.3. FESEM, EDX mapping and TEM analysis

The morphological features of GO, α-Fe$_2$O$_3$, PANI, and the 10PGF ternary composite are displayed in field emission scanning electron microscopy (FESEM) images (Fig. 3a–e). The SEM image of GO reveals thin, sheet-like structures, reflecting its layered configuration and substantial surface area, which is advantageous for offering abundant active sites (Fig. 3a). α-Fe$_2$O$_3$ (Fig. 3b) exhibits a structure with an elongated
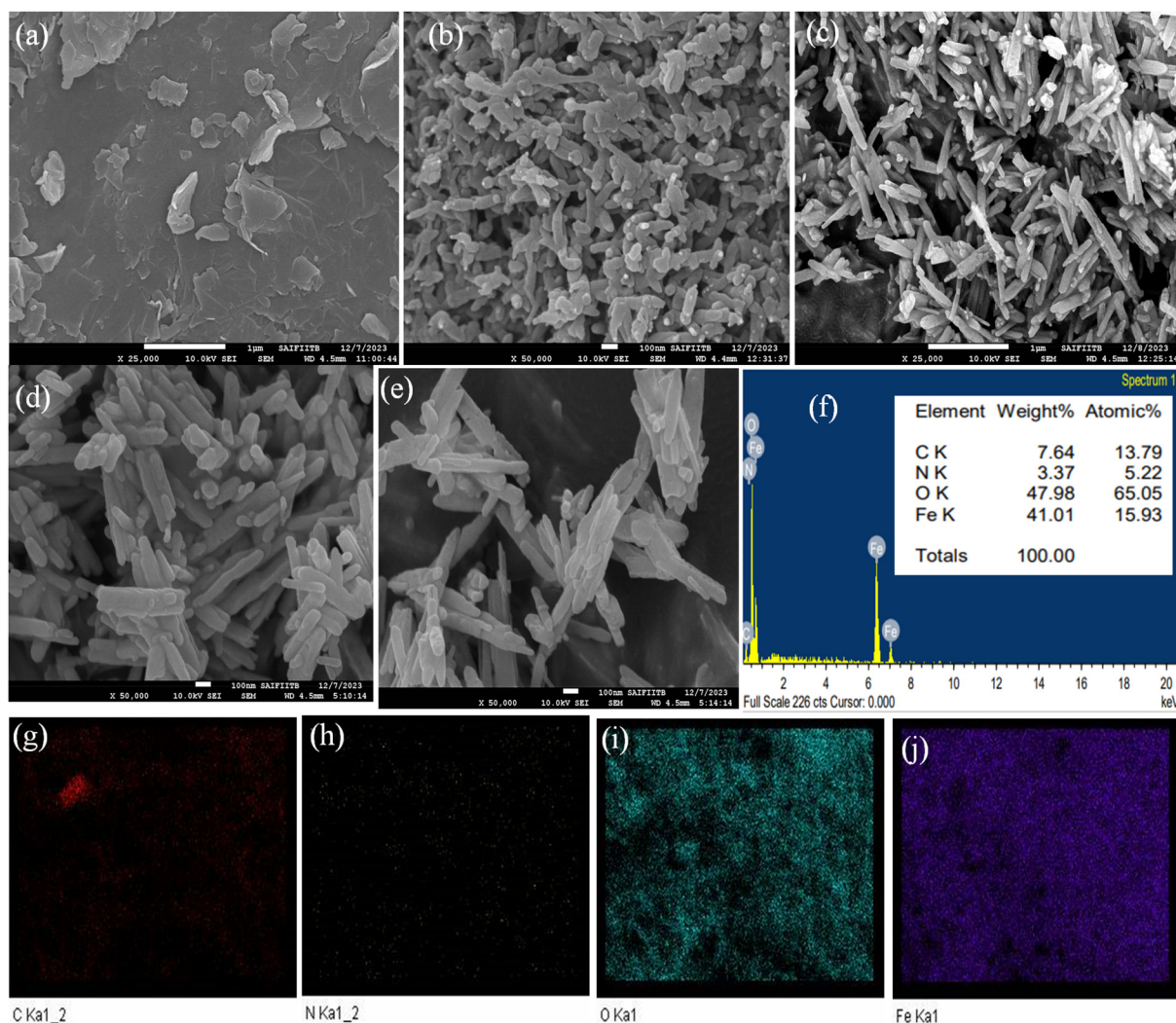

Fig. 3 FE-SEM images of GO (a), PANI (b), α-Fe$_2$O$_3$ (c), and the 10PGF ternary composite (d and e). EDX spectra with at% and wt% values of the elements (f) and elemental mapping of the 10PGF ternary composite (g–j).

nanorod shape with a rough texture, while PANI (Fig. 3c) reveals a porous, irregular X-shaped structure. The SEM images of the 10PGF ternary composite (Fig. 3d and e) depict a cohesive, interwoven structure where GO sheets form a conductive network, which could facilitate efficient charge transfer. As shown in Fig. 3f, EDX analysis identified the elements present in the 10PGF material. Elemental mapping in Fig. 3g–j further demonstrated the distribution of these elements (C, N, O, and Fe) within the 10PGF ternary composite. Transmission electron microscopy (TEM) offers detailed internal structural analysis, making it ideal for examining the fine-scale features and interfaces in composite materials. The TEM image of GO shown in Fig. 4a reveals a very thin sheet structure, whereas the TEM image of PANI shown in Fig. 4b displays an X-shaped structure with a rough surface. The rod-shaped morphology of α-Fe$_2$O$_3$, with coarse surfaces, is depicted in Fig. 4c. The high-resolution TEM images of 10PGF (Fig. 4d–f) emphasize the significant surface interactions within the composite. These images demonstrate an integrated 10PGF composite, showing a conductive network of GO that assists in efficient electron conduction and transfer.

3.4. XPS analysis

X-ray photoelectron spectroscopy (XPS) was used to determine the oxidation states and surface chemical environments of the elements, with both survey scans (Fig. S2†) and high-resolution spectra (Fig. 5) recorded for PANI, GO, α-Fe$_2$O$_3$, and the 10PGF ternary composite. The survey spectra (Fig. S2†) of 10PGF showed C, N, Fe and O, confirming the incorporation of pure materials (PANI, GO and α-Fe$_2$O$_3$) into the composite materials. The XPS spectrum of the C 1s region for the 10PGF composite shows three distinct peaks, each representing different carbon bonding states within the composite (Fig. 5a). These peaks suggest strong interactions, as indicated by shifts in the binding energies (BEs) of the C 1s peaks. The peak at 284.70 eV, indicating C–C or C=C bonds (sp^2 hybridized carbon atoms) typically found in GO, confirms the presence of the carbon framework. The peak at 285.60 eV is associated with carbon bonded to nitrogen, representing C–N or C=N bonds.[46] The peaks at 286.82 eV and 288.78 eV correspond to the C–O and C=O groups of carboxylic acid present in graphene oxide.[47] The high-resolution N 1s spectrum of the 10PGF ternary composite shows three peaks, each corresponding to different nitrogen environments in the polymer. The peak at 400.29 eV corresponds to benzenoid amine groups (–NH), representing the reduced form of PANI, while the peak at 401.84 eV corresponds to quinoid imine groups (–N=), representing the oxidized form of PANI. The peak at 402.67 eV indicates positively charged nitrogen species (–NH$^+$), arising from protonated amine groups within the PANI structure (Fig. 5b).[48] These BEs for the 10PGF ternary composite are higher than those observed in pure PANI. Similarly, the O 1s
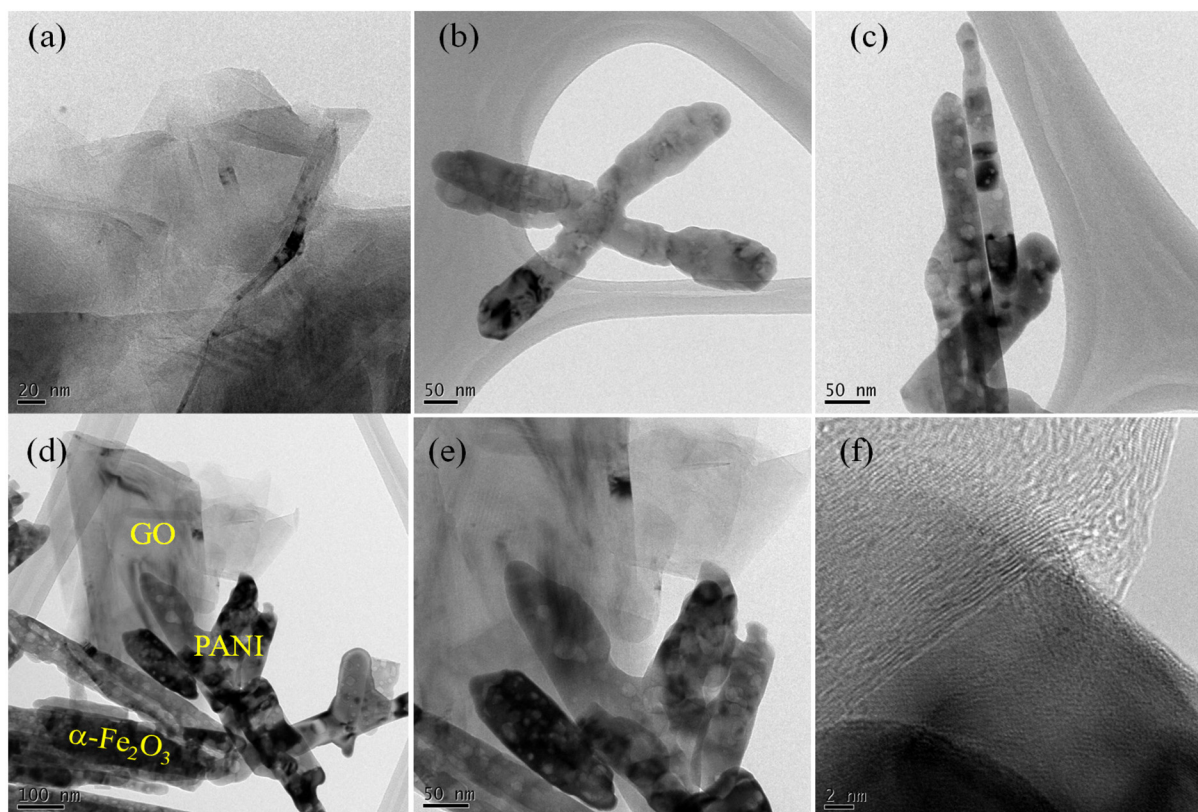

Fig. 4 TEM images of GO (a), PANI (b), α-Fe$_2$O$_3$ (c) and 10PGF (d–f).
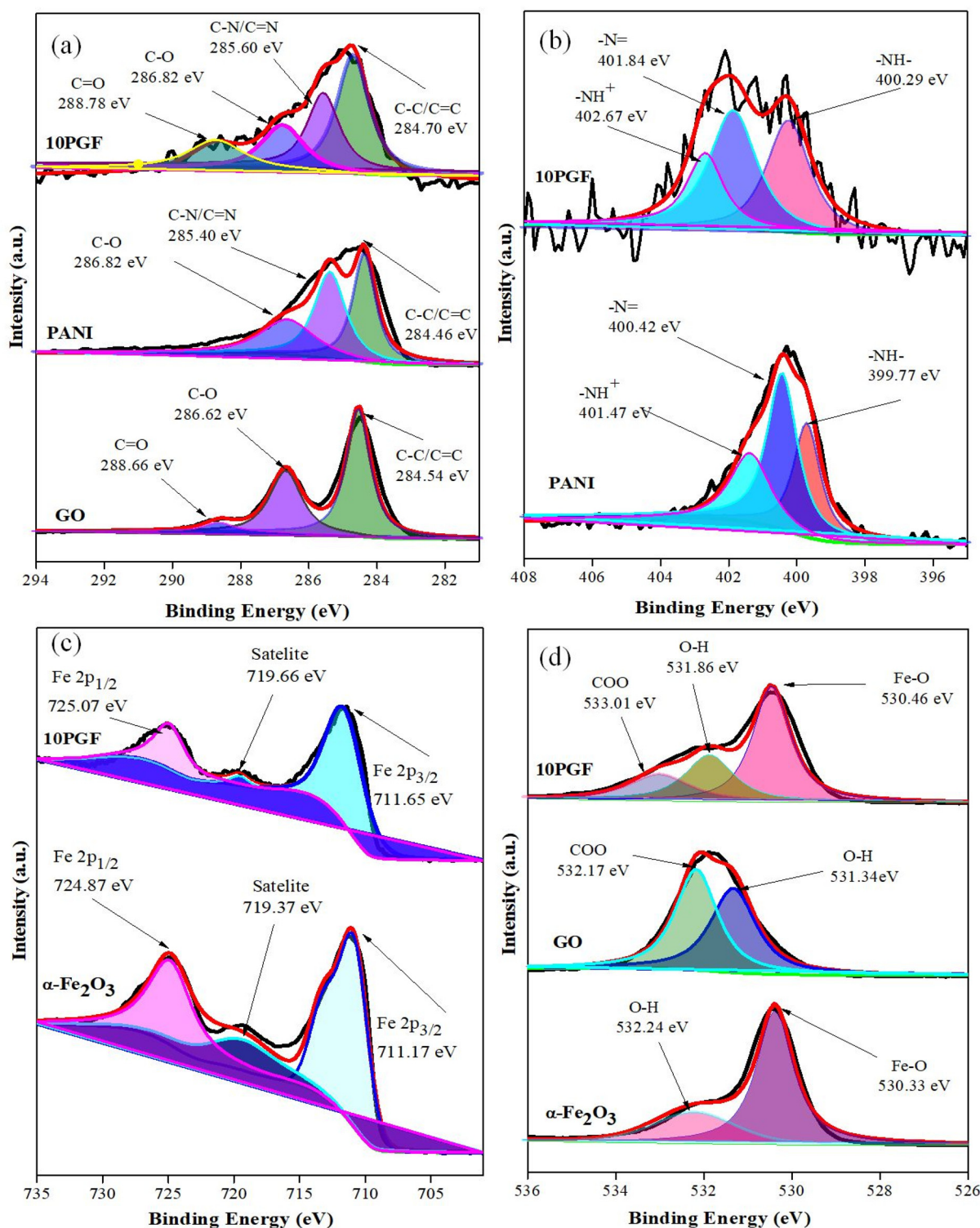
Fig. 5 High-resolution XPS spectra of pure PANI, GO, and α-Fe$_2$O$_3$ and the 10PGF ternary composite for C 1s (a), N 1s (b), Fe 2p (c), and O 1s (d).

spectrum of the 10PGF composite shows two main peaks, with shifts in BEs compared to pure materials. The dominant peak at 530.46 eV corresponds to lattice oxygen (O_2^-) in Fe–O bonds within the α-Fe$_2$O$_3$ structure, while a secondary peak at 531.86 eV is attributed to surface oxo and –OH groups, indicating the

presence of surface oxygen species and functional groups. A peak at 533.01 eV indicates the presence of –COO groups (Fig. 5d).[49] The Fe 2p spectrum of the 10PGF composite shows peaks at 711.65 eV and 725.07 eV, confirming iron in the +3 oxidation state typical of α-Fe$_2$O$_3$.[50] Furthermore, a satellite

peak at 719.66 eV confirms that Fe^{3+} ions are present in the composite (Fig. 5c). Strong interactions are indicated by these shifts in the Fe 2p BEs when compared to pure α-Fe_2O_3.[51] The successful incorporation of GO, PANI, and α-Fe_2O_3 into the 10PGF ternary composite was thus validated by the XPS analysis, which also showed notable BE changes, suggesting strong interactions between the constituents.

3.5. BET surface area analysis

Surface area properties of PANI, α-Fe_2O_3 and the 10PGF heterostructure were analyzed using the BET method, with the resulting BET surface area data and BJH pore size distributions presented in Fig. 6 and summarized in Table 1. The type IV isotherms observed are indicative of mesoporous materials, featuring pore sizes in the 5–6 nm range, while the H3 hysteresis loops suggest the presence of slit-shaped pores.[52] PANI and α-Fe_2O_3 have specific surface areas of 14.505 and 2.680 $m^2\,g^{-1}$,

Table 1 Textural properties of synthesized materials

Materials	S_{BET} ($m^2\,g^{-1}$)	Average pore size (nm)	Pore volume ($\times 10^{-2}\,cm^3\,g^{-1}$)
α-Fe_2O_3	2.6806	5.2051	0.2520
PANI	14.5050	5.7725	1.8051
10PGF	20.8024	5.3908	2.6092

respectively (Fig. 6a and b), while the 10PGF ternary composite shows a notable increase to 20.80 $m^2\,g^{-1}$ (Fig. 6c). This increase in the specific surface area is likely due to the increased interfacial interactions between PANI and α-Fe_2O_3 and the large surface area of GO. A larger surface area enhances the interaction between the photocatalyst and reactive species, while also boosting light absorption, thereby increasing the overall efficiency of the photocatalytic process.[53] Therefore, the increased specific surface area of the 10PGF
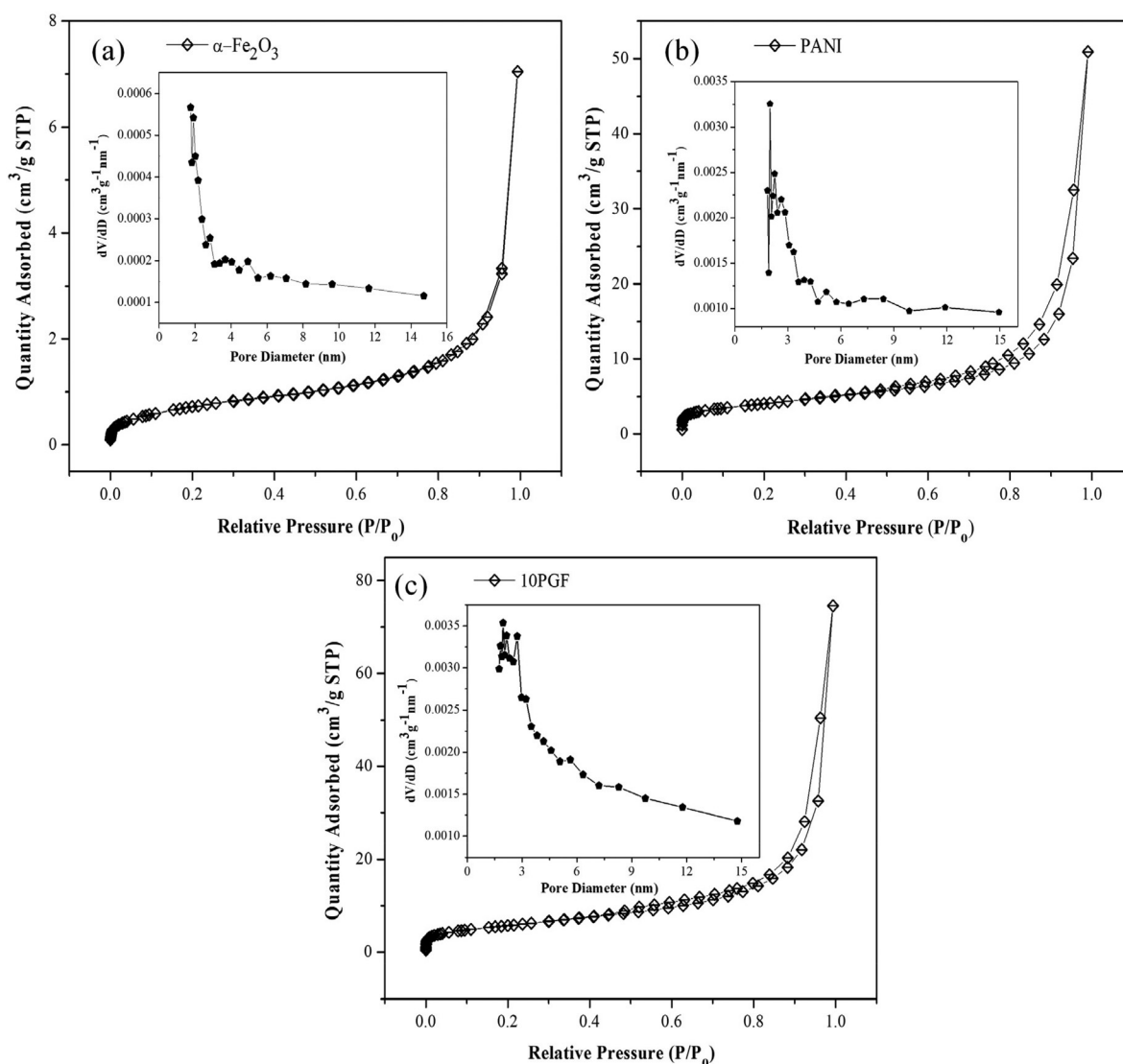

Fig. 6 Nitrogen adsorption–desorption isotherms for α-Fe_2O_3 (a), PANI (b) and 10PGF (c) and their pore size distribution curves (inset).

ternary composite is anticipated to greatly enhance its photo-catalytic efficiency for pollutant degradation.

3.6. Optical properties

The diffuse reflectance spectroscopy (DRS) spectra provide crucial insights into the light absorption properties and bandgap energies of the synthesized materials. Fig. 7a illustrates the DRS spectra for α-Fe_2O_3, PANI, and the 10PGF composite, depicting their optical characteristics within the 300–800 nm wavelength range. The absorption edge of α-Fe_2O_3 and PANI demonstrates strong absorptions in the visible light region (>500 nm). The broad absorption range observed with 10PGF suggests that the formation of heterojunctions within the composite significantly enhances its visible-light response. The bandgap energies (E_g) of both α-Fe_2O_3 and PANI can be determined using the Kubelka–Munk function, expressed as

$ah\nu = A(h\nu - E_g)^{n/2}$.[54] The exponent n, which depends on the semiconductor type, is set to 1 for direct transitions and 4 for indirect transitions.[55] Both α-Fe_2O_3 and PANI are indirect bandgap semiconductors with $n = 4$ for their absorption coefficient. To determine the bandgap energies (E_g), the values of $(ah\nu)^{1/2}$ and $(ah\nu)^2$ are plotted against photon energy ($h\nu$). As revealed in Fig. 7b, the calculated bandgap energies are 2.13 eV for α-Fe_2O_3, 2.34 eV for PANI (inset), and 2.07 eV for the 10PGF composite. Therefore, these observations confirmed that all the materials possess moderate band gaps and are active under visible light.

Photoluminescence (PL) spectra are crucial for studying the behavior of charge carriers in semiconductor materials, offering valuable insights into their dynamics, including processes like the recombination of electron–hole pairs ($e^- - h^+$) and the determination of the lifetime of photogenerated car-
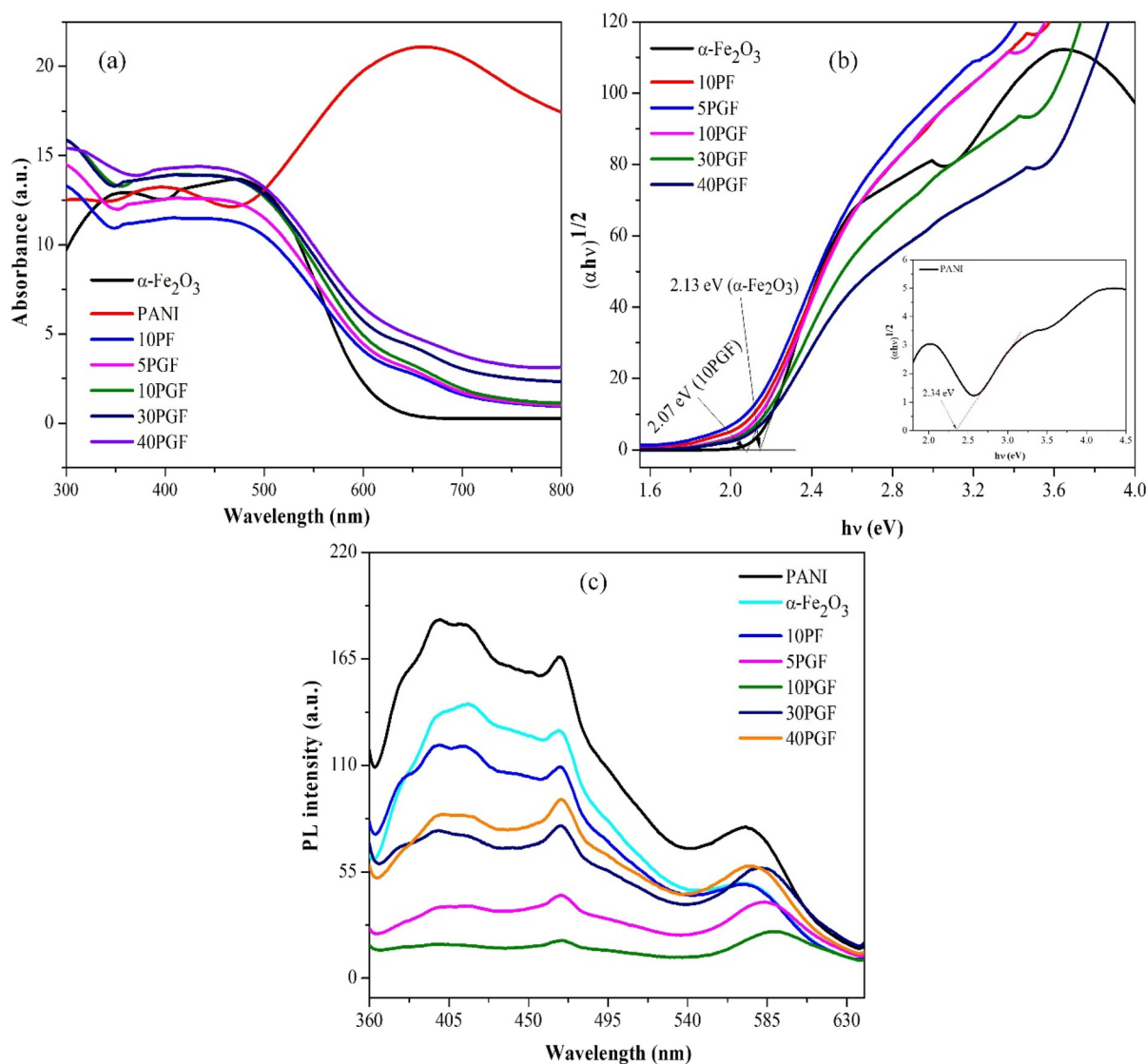

Fig. 7 UV–vis DRS spectra of pure α-Fe_2O_3, pure PANI, the 10PF binary composite and various ternary composites (a), the respective Tauc plots (b) and PL spectra of the photocatalysts (c).

riers.[56] When a semiconductor material is excited by an external light source, such as a laser, electron–hole pairs are generated in the material. The photoluminescence process involves the relaxation of these excited carriers to lower energy states, followed by the emission of photons as the carriers recombine.[57] In the presented study, the PL spectra, shown in Fig. 7c, highlight important findings. Pristine PANI displays a strong PL peak with a broad emission band near 450 nm, indicating a high rate of electron–hole recombination. Generally, lower PL intensity suggests a decreased rate of recombination, which is beneficial for higher photocatalytic activity in semiconductor materials.[58] Interestingly, the PL intensity of the 10PGF composite is considerably lower. This reduction can be ascribed to the synergistic interaction of these three components (PANI, GO, and α-Fe$_2$O$_3$), which effectively suppresses

e$^-$–h$^+$ recombination, improves charge carrier separation, and ultimately boosts photocatalytic efficiency.

3.7. Photocatalytic performances

The model organic compounds, BrG and CIP, were selected to estimate the photocatalytic effectiveness of the prepared composites, with the experimental results shown in Fig. 8. The UV-vis absorbance spectra for BrG and CIP are displayed in Fig. 8a and b, respectively. Fig. 8c and d illustrate the changes in the concentration of BrG and CIP over time when exposed to various photocatalysts, whereas Fig. 8e and f show the graphs of the total degradation percentages of BrG and CIP, respectively, over the same photocatalysts. Pure photocatalysts demonstrated limited effectiveness in pollutant removal, likely due to inefficient charge carrier separation as indicated by the PL
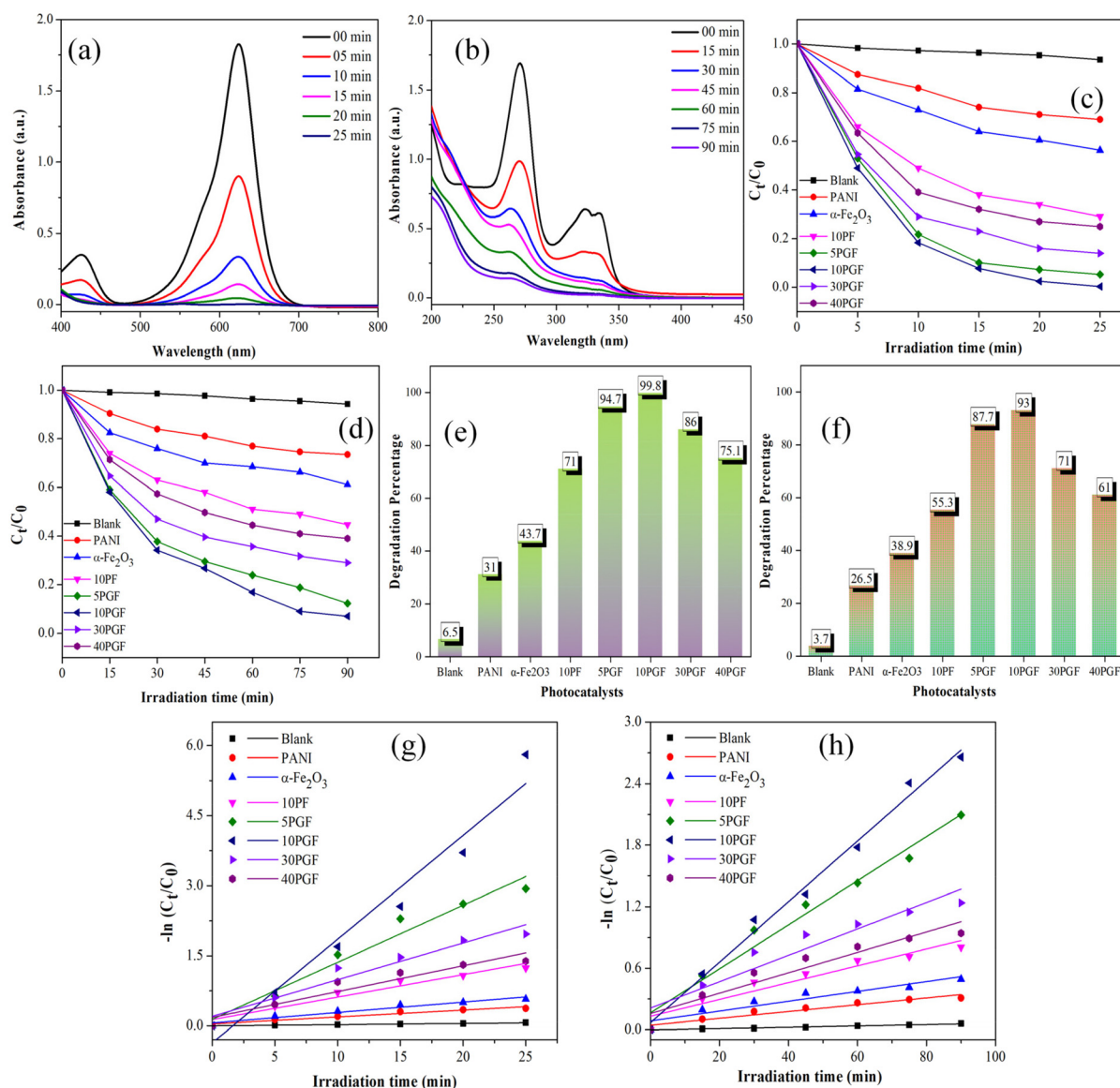

Fig. 8 Variations in the absorbance of BrG (a) and CIP (b) over 10PGF. Changes in the concentration of BrG (c) and CIP (d) and the overall degradation percentages of BrG (e) and CIP (f) under different photocatalytic conditions. Kinetics plots of BrG (g) and CIP (h) degradation.

analysis. α-Fe$_2$O$_3$ achieved approximately 43.7% degradation for BrG and 38.9% for CIP. Similarly, PANI achieved only 31% and 26.5% degradation for BrG and CIP, respectively, after 25 and 90 min of irradiation. Both BrG and CIP exhibited significant degradation when irradiated with the 10PGF composite. Notably, the 10PGF ternary heterostructure achieved over 99% removal of BrG within 25 min and 93% removal of CIP within 90 min of irradiation. These results emphasize the significant impact of the 10PGF composite on the degradation rates of BrG and CIP, highlighting its potential for enhanced performance under the given conditions. The incorporation of PANI into the 10PGF photocatalytic system significantly enhanced the efficiency of pollutant degradation, demonstrating its critical role in improving the overall photocatalytic performance. However, increasing the PANI ratio in the composites resulted in reduced degradation rates. The 30PGF nanocomposite achieved 86% and 71% degradation for BrG and CIP, respectively. The 40PGF composite reached 75.1% and 61% removal of BrG and CIP, respectively. The higher PANI content likely caused particle agglomeration in the ternary composite, reducing its efficiency in degrading pollutants. Nevertheless, all ternary composites were more effective than the 10PF binary composite, indicating that PANI further improved charge separation, facilitated by GO due to its excellent electron conductivity and efficient charge separation and transport capabilities.

The pseudo-first order rate equation provides for the determination of the degradation rate constants in an efficient manner,[59] even when the degradation process exhibits more complex behavior for BrG and CIP with the synthesized materials.[60] The plots obtained for kinetics showed that both of these pollutants degrade linearly, as depicted in Fig. 8g and h, respectively. The apparent rate constants (k) and corresponding R^2 values for all photocatalysts in the degradation of BrG and CIP are summarized in Tables S1 and S2,† respectively. The optimized 10PGF composite exhibited a rate constant (k) of approximately 0.222 min^{-1} for BrG, which is reported to be 15 times higher than that of PANI and 10 times higher than that of α-Fe$_2$O$_3$. The rate constant for CIP removal with 10PGF was 0.0295 min^{-1}, making it 8.9 times more effective than PANI and 6.1 times more effective than α-Fe$_2$O$_3$ photocatalysts.

3.8. Effect of operational parameters

3.8.1. Effect of the initial BrG concentration. This study investigated the degradation efficiency of the 10PGF composite with respect to the BrG dye at different concentrations. As shown in Fig. S3a,† the performance of the 10PGF ternary composite decreases as the initial BrG concentration increases. The results indicate that BrG dye at 5 ppm concentration is completely degraded within 15 min of irradiation. For BrG at 10 ppm concentration, the maximum degradation efficiency is reached in just 20 min of light exposure. With BrG at 15 ppm concentration, a degradation efficiency of 99.8% is achieved within 25 min of visible light irradiation. However, when the concentrations of BrG are further increased to 20, 25, 30, and

35 ppm, the degradation efficiency declines over a fixed dose of 0.9 g L^{-1} 10PGF ternary composite and a maximum irradiation time of 25 min. This decrease in efficiency could be due to the higher accumulation of BrG molecules, which reduces light penetration onto the surface of the 10PGF ternary composite.

3.8.2. Effect of the 10PGF ternary composite dosage. The impact of varying the dosage of the 10PGF composite was studied within a concentration range of 0.3–1.8 g L^{-1}, as illustrated in Fig. S3b.† With an increase in 10PGF concentration from 0.3 to 0.9 g L^{-1}, while maintaining a pH value of 7, a BrG concentration of 15 ppm, and an irradiation time of 25 min, the degradation efficiency increased from 43.2% to 99.8%. When the dosage was further increased to 1.2 g L^{-1}, nearly 100% degradation efficiency was achieved within 25 min of irradiation, likely due to an increase in the available active surface area. However, increasing the photocatalyst dose to 1.8 g L^{-1} resulted in a decrease in degradation efficiency to 93.3%, possibly due to the agglomeration of 10PGF composite materials and the subsequent reduction in light penetration.

3.9. Photostability and reusability

To evaluate the reusability of the 10PGF composite, a series of photocatalytic experiments was conducted, repeating the process 5 times under identical conditions (as illustrated in Fig. S4a†). The results showed that the efficiency of the 10PGF composite in the removal of BrG remained high throughout these cycles. Specifically, the degradation efficiency showed only a decline from an initial 99.8% to 92.9% after 5 consecutive uses. This slight decrease indicates that the 10PGF composite retains a high level of stability and efficiency in degrading pollutants over multiple cycles. To determine whether the photocatalyst experienced any structural alterations following repeated use, the XRD analysis was performed on the 10PGF composite. This analysis compared the diffraction patterns of the composite before and after undergoing 5 cycles of photocatalytic activity (Fig. S4b†). The lack of new or altered peaks in the XRD pattern suggests that the structural integrity of the 10PGF composite is well-preserved after the photocatalytic reactions.

3.10. Trapping studies and the photocatalytic mechanism

To elucidate the roles played by active species in the photodegradation facilitated by the 10PGF composite, trapping studies were conducted using specific scavengers, such as isopropanol (IPA) for the hydroxyl radicals ($^{\bullet}$OH), p-benzoquinone (BQ) for superoxide radicals ($O_2^{\bullet-}$), and EDTA-2Na for holes (h^+).[61–63] EDTA-2Na in the photocatalytic system led to a reduction of approximately 10% in the degradation efficiency of BrG compared to the system without any scavengers. This indicates a less significant role played by photogenerated holes in the degradation process. Similarly, the addition of IPA, which acts as a quencher for hydroxyl radicals, resulted in a noticeable decrease in degradation efficiency, with only 41.7% of BrG degradation achieved, emphasizing the critical involvement of hydroxyl radicals. The inclusion of BQ, which scavenges super-
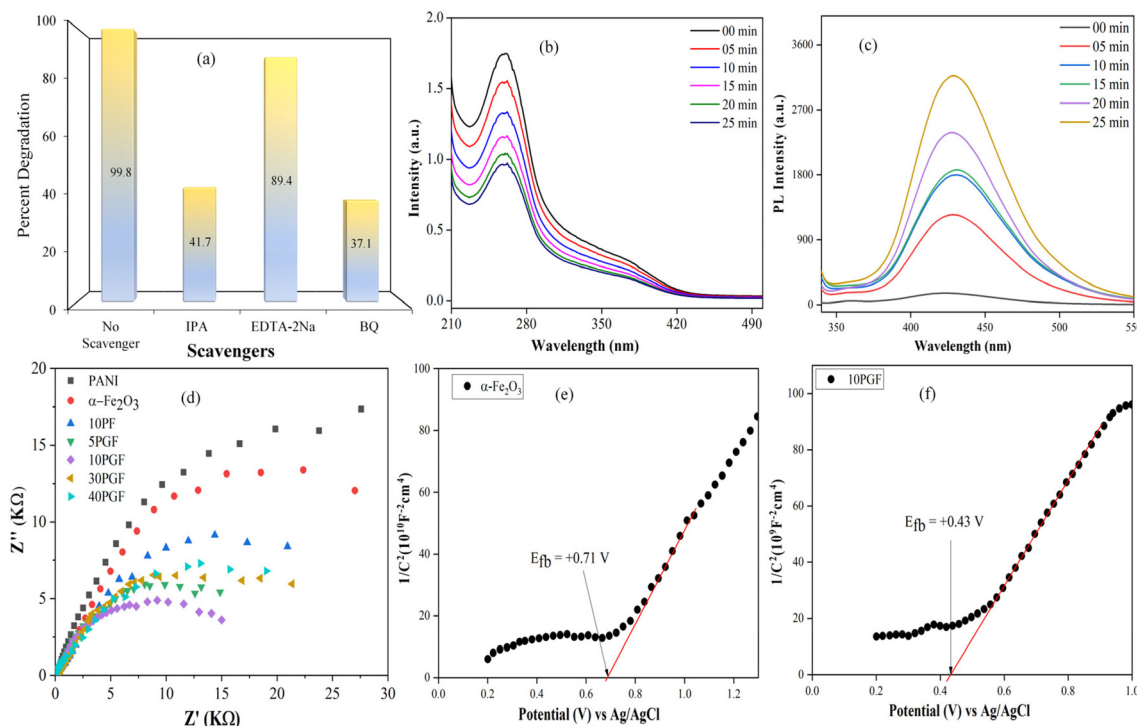
Fig. 9 Trapping experiment results (a), decrease in NBT spectra (b) and increase in the PL intensity of TA-OH (c) with the 10PGF composite. EIS Nyquist plots of all the photocatalysts (d); Mott–Schottky plots for α-Fe₂O₃ (e) and the 10PGF composite (f).

oxide radicals, caused a huge decrease in photocatalytic performance with about 37.1% BG degradation, highlighting the essential role of superoxide radicals in the 10PGF photocatalytic process. Further quantification of $O_2^{\bullet-}$ production was performed using the transformation of nitroblue tetrazolium (NBT) as a detection agent during the photocatalytic reaction.[64] As shown in Fig. 9b, a very high transformation of NBT was observed with the 10PGF composite, confirming its superior ability to generate superoxide radicals. To identify the presence of hydroxyl radicals, the terephthalic acid photoluminescence (TA-PL) probing method was utilized.[65] The reaction between terephthalic acid and hydroxyl radicals produces the highly fluorescent compound 2-hydroxyterephthalic acid (TAOH), allowing for effective detection and measurement of hydroxyl radicals.[66] The results, as presented in Fig. 9c, reveal the highest PL intensity for the 10PGF composite, further verifying the significant generation of hydroxyl radicals in this system.

Additionally, electrochemical impedance spectroscopy, which provides important information on how well interfacial charge transfer works in photocatalytic systems,[67] was carried out. The semicircular arc in EIS analysis represents charge transfer resistance, with a smaller arc radius indicating more efficient charge transfer.[68] Fig. 9d represents the EIS spectra of all the synthesized materials revealing that the 10PGF composite exhibits a notably smaller semicircular arc radius compared to that of pure PANI, pure α-Fe₂O₃, and the binary composite. This suggests that the 10PGF composite achieves more

effective separation of photogenerated electron–hole pairs and superior charge transport properties.

To validate the conduction band (CB) positions of α-Fe₂O₃ and the 10PGF ternary composite, Mott–Schottky (M–S) plots were recorded and analyzed. Furthermore, to establish the VB and CB potentials, the following equations were used:[69,70]

$$E_{CB} = X - E_e - 1/2E_g, \qquad (1)$$

$$E_{VB} = E_{CB} + E_g. \qquad (2)$$

Here, E_{VB} and E_{CB} denote the VB and CB potential, respectively. E_e signifies the energy level of a free electron on the H-scale (4.5 eV), E_g denotes the bandgap energy of the material, and X stands for the absolute electronegativity of the material:[71]

$$X = [\chi(A)^a \chi(B)^b \chi(C)^c]^{1/(a+b+c)}. \qquad (3)$$

Here, χ is the absolute electronegativity, and a, b, and c represent the number of atoms present in the synthesized materials.

The positive slope for α-Fe₂O₃, shown in Fig. 9e, indicates its behavior as an n-type semiconductor, with a flat band potential (E_{fb}) of +0.71 eV (vs. Ag/AgCl). For n-type semiconductors, E_{CB} is generally about 0.1 eV more negative than the E_{fb} value.[72] Thus, the CB value for α-Fe₂O₃ is determined to be 0.41 eV vs. the normal hydrogen electrode (NHE, where NHE = Ag/AgCl + 0.2 V). The E_{fb} value of the 10PGF ternary composite was found to be +0.43 eV, as depicted in Fig. 9f.

Previous reports indicate that the lowest unoccupied molecular orbital (LUMO) edge potential of PANI is −0.49 eV.[73] Considering this edge potential, the highest occupied molecular orbital (HOMO) of PANI is determined to be 1.85 eV. Applying the formula $E_{VB} = E_{CB} + E_g$, the E_{VB} of α-Fe$_2$O$_3$ is calculated to be 2.54 eV.

Based on these analyses, two potential charge transfer pathways can explain the photodegradation processes. In the conventional type II heterojunction mechanism (Fig. 10a), electrons from the LUMO of PANI transfer to the CB of α-Fe$_2$O$_3$ through the GO mediator, while holes from the VB of α-Fe$_2$O$_3$ migrate to the HOMO of PANI. As a result, electrons accumulate in the CB of α-Fe$_2$O$_3$, and holes gather in the HOMO of PANI. However, this mechanism is not consistent with the experimental results, as the CB electrons of α-Fe$_2$O$_3$ (0.41 V vs. NHE) are not sufficiently negative to generate superoxide radicals (O$_2^{\bullet-}$, −0.33 V vs. NHE).[74] Instead, a Z-scheme heterojunction mechanism is more plausible. In this model, electrons in the CB of α-Fe$_2$O$_3$ transfer to the HOMO of PANI via the GO mediator, where they recombine with holes. As depicted in Fig. 10b, this process allows electrons to accumulate in the LUMO of PANI with a reduction potential of −0.49 eV, which is sufficiently negative to reduce oxygen to superoxide radicals, consistent with the trapping experiments. The holes that accumulate in the VB of α-Fe$_2$O$_3$ can then directly oxidize water to hydroxyl radicals (2.40 V vs. NHE).[75]
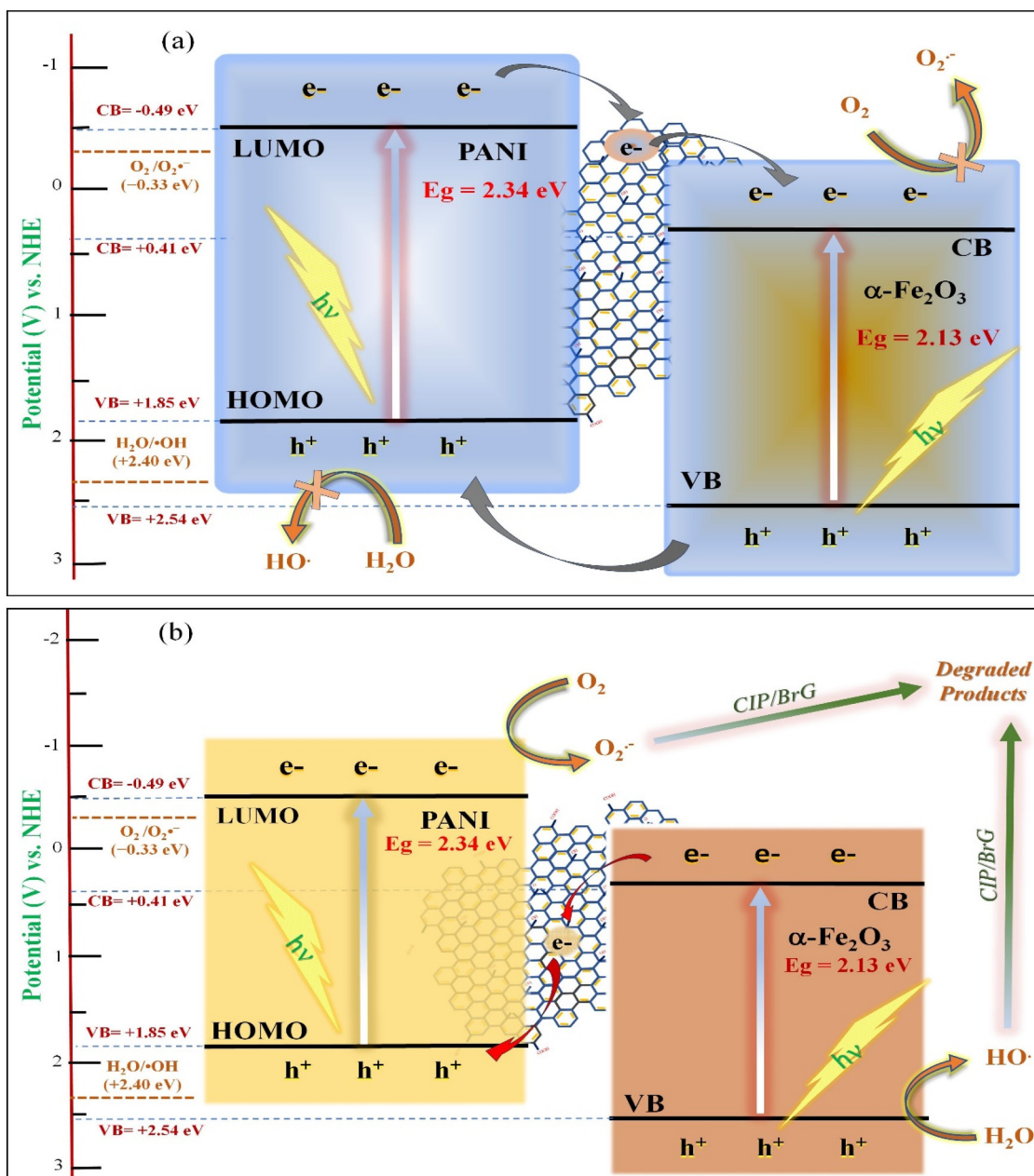

Fig. 10 Conventional mechanism (a) and Z-scheme mechanism (b) for the 10PGF heterostructure.

Consequently, the resulting hydroxyl radicals and superoxide radicals contribute to the degradation of pollutants in the 10PGF photocatalytic system. These findings collectively suggest that the degradation of organic pollutants over the 10PGF composite occurs *via* a Z-scheme reaction mechanism.

4. Adsorption studies

4.1. Adsorption isotherms

Adsorption isotherm studies were performed using the Langmuir and Freundlich models to evaluate the ability of 10PGF composites to adsorb the BrG dye. The equilibrium concentration of BrG in the liquid phase and the amount adsorbed on the 10PGF surface were analyzed to evaluate the adsorption capacity. The Langmuir model and Freundlich model are represented by eqn (4) and (5), respectively:[76]

$$q_e = \frac{q_m K_L C_e}{1 + K_L C_e} \tag{4}$$

$$q_e = K_F C_e^{1/n}. \tag{5}$$

The Langmuir and Freundlich plots are given in Fig. 11a and the estimated parameters calculated from these models for adsorption of BrG onto 10PGF are given in Table S3.† The experimental data showed a strong correlation with the Langmuir isotherm, with an R^2 value of 0.974. This model revealed a maximum adsorption capacity (q_m) of 28.97 mg g^{-1}, suggesting monolayer adsorption on the surface of the adsorbent.[77] Conversely, the Freundlich model provided an R^2 value of 0.9559 and a K_F (Freundlich constant) value of 15.17, suggesting that while adsorption follows this model, the Langmuir model is more dominant. The slope ($1/n$) in the Freundlich isotherm equation, being less than 1, indicates a favorable chemisorption process.[78] Additionally, the favorabil-

ity of the adsorption process was confirmed by the equilibrium parameter (R_L) as shown in eqn (6):

$$R_L = \frac{1}{1 + K_L C_0} \tag{6}$$

where K_L is the Langmuir adsorption equilibrium constant, reflecting the affinity between the adsorbent and the adsorbate and C_0 is the initial concentration of the adsorbate in the solution. The R_L values, tabulated in Table S4,† are in the range of 0 to 0.15 indicating favorable adsorption.[79] Therefore, the Langmuir model is more appropriate for describing the adsorption behavior of the BrG dye on the 10PGF adsorbent.

4.2. Adsorption kinetics studies

The kinetics of BrG adsorption on the 10PGF adsorbent was studied to estimate the amount of dye adsorption over time. The kinetics analysis was performed through nonlinear fittings utilizing the following two models as described by eqn (7) and (8), respectively:[80]

Pseudo-first order (PFO) model

$$q_t = q_e(1 - e^{-K_1 t}). \tag{7}$$

Pseudo-second order (PSO) model

$$q_t = \frac{K_2 q_e^2 t}{1 + K_2 q_e t} \tag{8}$$

From the plots (Fig. 11b) and the determined values (tabulated in Table S5†), it is observed that the pseudo-first order model fitted the data well, as indicated by a good R^2 value of 0.94274. However, the PSO model provided a much better fit with an R^2 value of 0.98892. The low error function value (red curve, $\chi^2 = 0.15074$) further validated the PSO kinetics as the most appropriate model for predicting adsorption kinetics in this system.
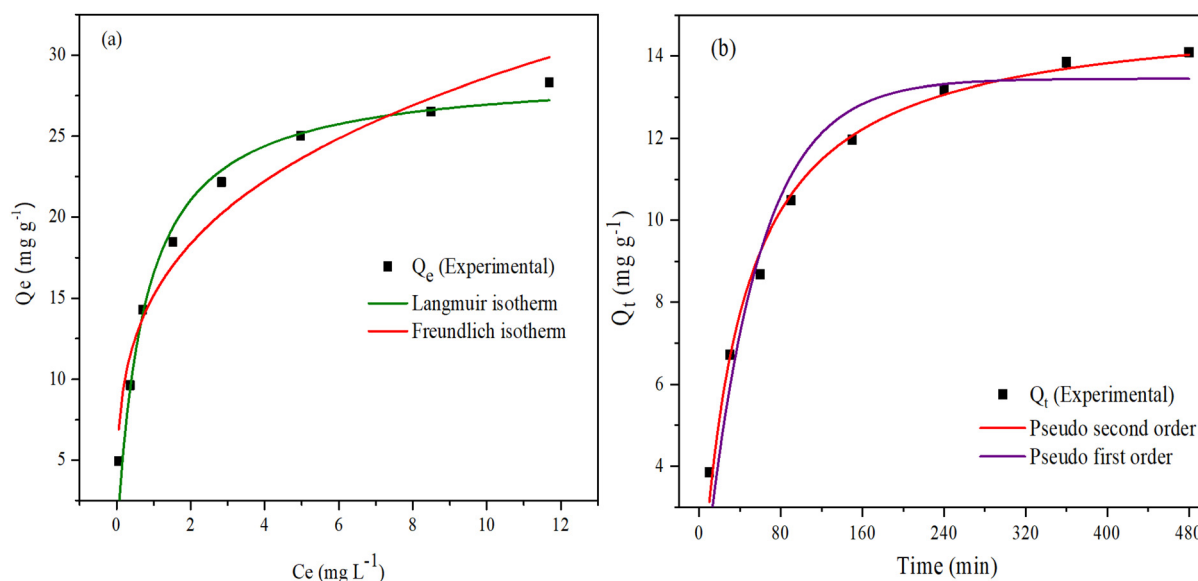

Fig. 11 Plots of adsorption isotherms (Langmuir and Freundlich) (a) and BrG adsorption kinetics over the 10PGF ternary composite (b).

5. Conclusion

This study successfully synthesized a novel Z-scheme ternary heterostructure consisting of PANI, GO and α-Fe$_2$O$_3$. The structural and morphological characterization confirmed the formation of the composite, with significant interactions among its components. The increased BET surface area of the 10PGF composite facilitates more active sites for photocatalytic reactions. The composite exhibited exceptional photocatalytic activity under visible light, achieving 99.8% degradation of BrG and 93% of CIP within irradiation times of 25 and 90 min, respectively. This remarkable performance is attributed to the synergistic effects of PANI, GO, and α-Fe$_2$O$_3$, which enhance charge separation and reduce electron–hole recombination, as confirmed by PL and EIS analyses. The 10 PGF composite demonstrated strong recyclability, maintaining high efficiency over 5 cycles without significant structural changes. Trapping experiments highlighted the critical roles of O$_2^{\bullet-}$ and $^{\bullet}$OH in the photocatalytic degradation process, supporting a Z-scheme mechanism where efficient charge transfer occurs *via* GO. Adsorption studies revealed that the 10PGF composite closely follows the Langmuir isotherm and PSO kinetics, suggesting monolayer adsorption and chemisorption processes.

Data availability

All additional data are available in the ESI.†

Conflicts of interest

The authors declare that they have no known competing financial interests or personal relationships that could have appeared to influence the work reported in this paper.

Acknowledgements

References

1 L. Wang, X. Min, X. Sui, J. Chen and Y. Wang, *J. Colloid Interface Sci.*, 2020, **560**, 21–33.
2 B. Shao, X. Liu, Z. Liu, G. Zeng, W. Zhang, Q. Liang, Y. Liu, Q. He, X. Yuan, D. Wang, S. Luo and S. Gong, *Chem. Eng. J.*, 2019, **374**, 479–493.
3 E. E. El-Katori, M. A. Ahmed, A. A. El-Bindary and A. M. Oraby, *J. Photochem. Photobiol., A*, 2020, **392**, 112403.
4 B. Liu, X. Hu, J. Yang, C. Yang and Y. Huang, *Catal. Sci. Technol.*, 2022, **13**, 504–515.
5 N. R. Reddy, A. S. Kumar, P. M. Reddy, D. Merum, R. R. Kakarla, J. H. Jung, S. W. Joo and T. M. Aminabhavi, *J. Environ. Manage.*, 2023, **332**, 117397.
6 S. A. Mirsalari and A. Nezamzadeh-Ejhieh, *Mater. Sci. Semicond. Process.*, 2021, **122**, 105455.
7 A. Nezamzadeh-Ejhieh and E. Shahriari, *Int. J. Photoenergy*, 2011, **2011**, 518153.
8 P. Hemmatpour and A. Nezamzadeh-Ejhieh, *Chemosphere*, 2022, **307**, 135925.
9 E. Shahnazari-Shahrezaie and A. Nezamzadeh-Ejhieh, *RSC Adv.*, 2017, **7**, 14247–14253.
10 H. Derikvandi and A. Nezamzadeh-Ejhieh, *J. Hazard. Mater.*, 2017, **321**, 629–638.
11 W. Wang, D. Ma, Y. Dai, Q. Wang, H. Xu, C. Yuan, X. Zhang, P. Dong and X. Xi, *Colloids Surf., A*, 2023, **675**, 131938.
12 A. Kumar, S. K. Sharma, G. Sharma, A. H. Al-Muhtaseb, M. Naushad, A. A. Ghfar and F. J. Stadler, *J. Hazard. Mater.*, 2019, **364**, 429–440.
13 Z. Rasool, M. S. Athar and M. Muneer, *Environ. Sci. Pollut. Res.*, 2024, **31**, 31259–31272.
14 A. A. Hoseini, S. Farhadi, A. Zabardasti and F. Siadatnasab, *RSC Adv.*, 2019, **9**, 24489–24504.
15 M. S. Athar and M. Muneer, *Photochem. Photobiol. Sci.*, 2023, **22**, 695–712.
16 H. Liu, M. Hou, H. Fu, A. Hu, Y. Zhai, L. Wang, D. Zhai, S. Zhang and S. Wang, *Surf. Interfaces*, 2024, **44**, 103795.
17 D. R. Rout and H. M. Jena, *J. Taiwan Inst. Chem. Eng.*, 2023, **147**, 104914.
18 S. Salesi and A. Nezamzadeh-Ejhieh, *Environ. Sci. Pollut. Res.*, 2023, **30**, 105440–105456.
19 L. Wang, Z. Li, J. Chen, Y. Huang, H. Zhang and H. Qiu, *Environ. Pollut.*, 2019, **249**, 801–811.
20 H. A. Bicalho, R. D. F. Rios, I. Binatti, J. D. Ardisson, A. J. Howarth, R. M. Lago and A. P. C. Teixeira, *J. Hazard. Mater.*, 2020, **400**, 123310.
21 R. Lei, H. Ni, R. Chen, H. Gu, B. Zhang and W. Zhan, *J. Colloid Interface Sci.*, 2018, **514**, 496–506.
22 M. Tong, D. Sun, R. Zhang, H. Liu and R. Chen, *J. Alloys Compd.*, 2021, **862**, 158271.
23 Z. Masoumi, M. Tayebi and B. Lee, *Ultrason. Sonochem.*, 2020, **72**, 105403.
24 F. Wang, X. Yu, M. Ge and S. Wu, *Chem. Eng. J.*, 2020, **384**, 123381.
25 S. M. Botsa, G. P. Naidu, M. Ravichandra, S. J. Rani, R. B. Anjaneyulu and C. V. Ramana, *J. Mater. Res. Technol.*, 2020, **9**, 12461–12472.
26 F. Li, X. Li, S. Tong, J. Wu, T. Zhou, Y. Liu and J. Zhang, *Nano Energy*, 2023, **117**, 108849.
27 S. P. Keerthana, R. Yuvakkumar, G. Ravi, P. Kumar, M. S. Elshikh, H. H. Alkhamis, A. F. Alrefaei and D. Velauthapillai, *Chemosphere*, 2021, **270**, 129498.
28 J. Jiang, J. Gao, T. Li, Y. Chen, Q. Wu, T. Xie, Y. Lin and S. Dong, *J. Colloid Interface Sci.*, 2019, **554**, 531–543.
29 L. Zhang, X. Zhang, C. Wei, F. Wang, H. Wang and Z. Bian, *Chem. Eng. J.*, 2022, **435**, 134873.

30 M. S. Athar and M. Muneer, *J. Alloys Compd.*, 2023, **980**, 173385.

31 I. Ahmad, M. Saud, M. Muneer, H. M. Altass, R. F. Felemban and S. A. Ahmed, *Surf. Interfaces*, 2024, **45**, 103819.

32 F. Y. Liu, Y. M. Dai, F. H. Chen and C. C. Chen, *J. Colloid Interface Sci.*, 2020, **562**, 112–124.

33 S. Qu, Y. Xiong and J. Zhang, *Sep. Purif. Technol.*, 2019, **210**, 382–389.

34 M. G. Hosseini, P. Y. Sefidi, A. M. Mert and S. Kinayyigit, *J. Mater. Sci. Technol.*, 2020, **38**, 7–18.

35 F. Akti, *Appl. Surf. Sci.*, 2018, **455**, 931–939.

36 A. Verma and R. Bilash, *J. Inorg. Organomet. Polym. Mater.*, 2019, **29**, 444–455.

37 P. Hait, R. Mehta and S. Basu, *J. Cleaner Prod.*, 2023, **424**, 138851.

38 A. Meftahi, M. Shabani-Nooshabadi and A. Reisi-Vanani, *J. Energy Storage*, 2023, **63**, 107077.

39 Q. Q. Xu, W. Huo, S. S. Li, J. H. Fang, L. Li, B. Y. Zhang, F. Zhang, Y. X. Zhang and S. W. Li, *Appl. Surf. Sci.*, 2020, **533**, 1–9.

40 C. Munikrishnappa, S. Kumar, S. Shivakumara, G. M. Rao and N. Munichandraiah, *J. Sci.: Adv. Mater. Devices*, 2019, **4**, 80–88.

41 S. Chen, D. Huang, G. Zeng, W. Xue, L. Lei, P. Xu, R. Deng, J. Li and M. Cheng, *Chem. Eng. J.*, 2020, **382**, 122840.

42 P. Y. Wong, S. W. Phang and A. Baharum, *RSC Adv.*, 2020, **10**, 39693–39699.

43 N. D. Sonwane and S. B. Kondawar, *Mater. Lett.*, 2021, **303**, 130566.

44 S. Sobhanardakani, A. Jafari, R. Zandipak and A. Meidanchi, *Process Saf. Environ. Prot.*, 2018, **120**, 348–357.

45 N. Sabah Ahmed, C. Y. Hsu, Z. H. Mahmoud, H. Sayadi and E. Kianfar, *RSC Adv.*, 2023, **13**, 36280–36292.

46 D. A. Pethsangave, R. V. Khose, P. H. Wadekar, D. K. Kulal and S. Some, *ChemistrySelect*, 2020, **5**, 1516–1525.

47 B. Zhan, Y. Liu, W. T. Zhou, S. Y. Li, Z. B. Chen, T. Stegmaier, M. Aliabadi, Z. W. Han and L. Q. Ren, *Appl. Surf. Sci.*, 2021, **541**, 148638.

48 F. Liu, S. Luo, D. Liu, W. Chen, Y. Huang, L. Dong and L. Wang, *ACS Appl. Mater. Interfaces*, 2017, **9**, 33791–33801.

49 W. C. Oh, K. N. Fatema, Y. Liu, C. S. Lim, K. Y. Cho, C. H. Jung and M. R. U. D. Biswas, *J Photochem. Photobiol., A*, 2020, **394**, 112484.

50 S. Yan, Y. Shi, Y. Tao and H. Zhang, *Chem. Eng. J.*, 2019, **359**, 933–943.

51 M. S. Athar, A. Khan, I. Ahmad and M. Muneer, *New J. Chem.*, 2024, **48**, 5346–5361.

52 M. K. Kesarla, M. O. Fuentez-Torres, M. A. Alcudia-Ramos, F. Ortiz-Chi, C. G. Espinosa-González, M. Aleman, J. G. Torres-Torres and S. Godavarthi, *J. Mater. Res. Technol.*, 2019, **8**, 1628–1635.

53 H. Li, D. Wang, C. Miao, F. Xia, Y. Wang, Y. Wang, C. Liu and G. Che, *J. Environ. Chem. Eng.*, 2022, **10**, 108201.

54 M. S. Athar, N. Saleem, I. Ahmad, M. Fazil, T. Ahmad and M. Muneer, *Mater. Today Sustainability*, 2024, **26**, 100779.

55 K. Ouyang, C. Yang, B. Xu, H. Wang and S. Xie, *Colloids Surf., A*, 2021, **625**, 126978.

56 M. Rezaei, A. Nezamzadeh-Ejhieh and A. R. Massah, *ACS Omega*, 2024, **9**, 6093–6127.

57 P. Mohammadyari and A. Nezamzadeh-Ejhieh, *RSC Adv.*, 2015, **5**, 75300–75310.

58 M. Chatterjee, M. Mondal, T. Sukul, K. Ghosh and S. K. Pradhan, *J. Ind. Eng. Chem.*, 2023, **127**, 390–405.

59 P. Ghahremani, M. H. Vakili and A. Nezamzadeh-Ejhieh, *J. Environ. Chem. Eng.*, 2021, **9**, 106648.

60 C. T. Haile, N. Ahmad, C. W. Chiu and C. F. J. Kuo, *Chemosphere*, 2023, **323**, 138108.

61 X. Yu, J. Zhang, Y. Chen, Q. Ji, Y. Wei, J. Niu, Z. Yu and B. Yao, *J. Environ. Chem. Eng.*, 2021, **9**, 106161.

62 I. Ahmad and M. Muneer, *Colloids Surf., A*, 2024, **702**, 135066.

63 X. Yu, H. Chen, Q. Ji, Y. Chen, Y. Wei, N. Zhao and B. Yao, *Chemosphere*, 2020, **267**, 129285.

64 M. Danish, M. S. Athar, I. Ahmad, M. Z. A. Warshagha, Z. Rasool and M. Muneer, *Appl. Surf. Sci.*, 2022, **604**, 154604.

65 S. Ghattavi and A. Nezamzadeh-Ejhieh, *Catal. Sci. Technol.*, 2023, **13**, 737–749.

66 H. Yin, C. Yuan, H. Lv, K. Zhang, X. Chen and Y. Zhang, *Sep. Purif. Technol.*, 2023, **308**, 122815.

67 M. Nosuhi and A. Nezamzadeh-Ejhieh, *New J. Chem.*, 2017, **41**, 15508–15516.

68 X. Yu, J. Zhang, J. Zhang, J. Niu, J. Zhao, Y. Wei and B. Yao, *Chem. Eng. J.*, 2019, **374**, 316–327.

69 M. Farsi and A. Nezamzadeh-Ejhieh, *Surf. Interfaces*, 2022, **32**, 102148.

70 M. S. Athar, Z. Rasool, M. Muneer, H. M. Altass, I. I. Althagafi and S. A. Ahmed, *ACS Omega*, 2023, **8**(41), 38272–38287.

71 S. Ghattavi and A. Nezamzadeh-Ejhieh, *Composites, Part B*, 2020, **183**, 107712.

72 W. Chen, L. Li, L. Li, W. Qiu, L. Tang, L. Xu and K. Xu, *Engineering*, 2019, **5**, 755–767.

73 R. Zhang, Q. Han, Y. Li, T. Zhang, Y. Liu, K. Zeng and C. Zhao, *Sep. Purif. Technol.*, 2019, **7**, 116098.

74 I. Ahmad, M. Muneer, A. S. Khder and S. A. Ahmed, *ACS Omega*, 2023, **8**(25), 22708–22720.

75 Y. Yan, X. Zhou, P. Yu, Z. Li and T. Zheng, *Appl. Catal., A*, 2020, **590**, 117282.

76 M. F. Dapaah, B. Liu and L. Cheng, *J. Environ. Chem. Eng.*, 2021, **9**, 105275.

77 T. H. Pham, S. H. Jung, Y. J. Kim and T. Y. Kim, *Chemosphere*, 2021, **268**, 129319.

78 K. S. Bhavsar, P. K. Labhane, V. R. Huse, R. B. Dhake and G. H. Sonawane, *Inorg. Chem. Commun.*, 2020, **121**, 108215.

79 Y. Cardona, S. A. Korili and A. Gil, *Chem. Eng. J.*, 2021, **425**, 130708.

80 L. Yao, L. Zhang, B. Long, Y. Dai and Y. Ding, *J. Mol. Liq.*, 2021, **325**, 115002.